Misalignment error analysis in polychromatic division of focal plane Stokes polarimeters

ANGEL LIZANA,[1,*] [iD] JUAN CAMPOS,[1] [iD] ALBERT VAN EECKHOUT,[1] [iD] AND ANDRÉS MARQUEZ[2] [iD]

[1]*Departamento de Física, Universitat Autònoma de Barcelona, Bellaterra, 08193, Spain*
[2]*Dept. de Física, Ingeniería de Sistemas y Teoría de la Señal, Universidad de Alicante, Ap. 99, Alicante, 03080, Spain*
*angel.lizana@uab.es

Abstract: Snapshot imaging polarimeters are used in many different areas. Recently, division of focal plane (DoFP) polarimeters have proved useful as snapshot polarimeters for dynamic applications. For an optimal performance of polarimeters, different works dealing with the error analysis of such devices are proposed in literature. In terms of noise amplification from intensity measurements to the final polarization calculations, well-established quality metrics, as in the condition number or the equally weighted variance criteria, are used. Other studies analyze systematic errors due to deviations in the construction parameters. However, something not considered so far is the effect produced by misalignment between the various pixelated masks over the pixelated structure of the camera sensor, always occurring in experimental implementations of DoFPs. In this work, we study the effect of such misalignments in DoFP polarimeters and demonstrate how they lead to polarimetric systems composed of partially depolarized analyzers. We calculate the combined degree of polarization related to different amounts of misalignment and analyze the corresponding system performance. From this study, we show how an imaging polarimeter based on partially polarized analyzers can still lead to a robust and accurate polarimetric performance, and we also provide the misalignment limits in which an acceptable performance is obtained. We evaluate both the monochromatic and the polychromatic cases with special focus on the latter.

1. Introduction

The state of polarization (SOP) provides great deal of information about light-matter interactions. There is a large interest in the use of polarimetric information in many applications including biomedical physics [1–3], astronomy [4,5], polarizing sample characterization [6–8], among others. Conventional optical imaging is typically restricted to the use of light field intensity information. Spectroscopic systems also include the characteristic wavelength of light. However, the use of polarimetric information is opening new possibilities in the various areas mentioned before and in many others, which has prompted the proposal of different polarimetric imaging cameras, i.e. imaging polarimeters. Some categories are considered in the literature [9], as division of time polarimeters (DoTP), amplitude (DoAmP), aperture (DoAP), and focal-plane (DoFP). Our main interest in the paper are focal-plane imaging polarimeters which offer serious advantages, such as robust design, small size and dynamic acquisition [10–17], enabling for snapshot polarimetry.

DoFPs can be divided in two categories depending on if they offer partial or complete Stokes polarization information. In the former case, a micropolarizer array (MPA) [11–13] is usually attached to the camera sensor and the pixels of both the MPA and the sensor are aligned. The first three Stokes components are measured in the image, which is sufficient for some applications. In the complete Stokes case, Kikuta *et al.* built a DoFP able to fully characterize light polarization thanks to the inclusion of a birefringence microretarder based on subwavelength gratings [14].

Since then various designs were proposed and/or implemented [10,15–17]. Hsu et al. [10] fabricated a DoFP based on a patterned liquid crystal polymer (LCP) microretarder layer, an isolation layer, and a uniform LCP polarizer. Zhao *et al.* [15] demonstrated a system based on patterning a liquid-crystal (LC) layer on top of a visible-regime metal-wire-grid polarizer. Then, Gu *et al.* [17] analyzed a design based on an encoded birefringent crystal and a MPA.

For a complete Stokes vector characterization a minimum of four independent polarization analyzers are necessary, which produces a 4×4 square measurement matrix [18] associated with the polarimeter. The polarimeters noise amplification from intensity measurements to the Stokes vector calculation is given by the condition number (CN) [19] of the particular polarimeter measurement matrix, which considers how well defined is this matrix to inversion. In the case of redundant measurements, i.e. more than four polarization analyzers, the equally weighted variance (EWV) [18,19] is a more appropriate figure of merit. Related parameters are the sensitivity of the Stokes parameters to noise, which can be used to assess if error amplification depends on the specific SOP measured [18].

Systematic errors due to deviations in the construction parameters (retardation, orientation of neutral lines, etc.) are also usually analyzed [10,15,17]. An analysis of the bandwidth tradeoffs, error performance, and noise resiliency of full-Stokes micropolarizer array (MPA) designs was also provided in Ref. [20]. However, something not considered is the effect produced by misalignment between the various pixelated masks over the pixelated structure of the camera sensor, always occurring in experimental implementations. This misalignment generates a spatially incoherent sum of polarized light, which results in a finite degree of unpolarized light incident onto the pixels of the camera sensor. The system is thus working as composed of a set of partially depolarized analyzers, produced by this spatial averaging. Therefore, the question that comes into play is: what is the performance of a Stokes polarimeter with polarization analyzers partially depolarized?. Even knowing that it is never beneficial to use partially polarized illumination or analysis for polarimetry [21], we want to study if DoFP based on partial polarized analyzers, which arise from spatial misalignments, can still lead to polarimeters with acceptable performance.

The outline of this work is as follows. In Section 2 we mathematically describe how spatial misalignments increase the depolarization content of resulting polarization analyzers. In Section 3, the effect of these partial analyzers in the performance of the resultant polarimeter is thoroughly studied through a series of simulations. The monochromatic and polychromatic cases are both provided in Subsections 3.1 and 3.2, respectively. In addition, a robustness study to manufacturing errors is also given in Subsection 3.3. Finally, the main conclusions of the work are given in Section 4.

2. Misalignment effect on a DoFP polarimeter: partially polarized analyzers

Let us consider a specific model from which to build the analysis. The SOP of light can be described by the Stokes vector $\vec{S}$, consisting of four components (S_0, S_1, S_2, S_3). To obtain the values for the four components a minimum of four independent measurements are necessary. In DoFP imaging polarimeters, this means examining the intensity values of four neighboring pixels of the camera sensor. This collection of four intensity measurements arises from the projection of the local input polarization on the DoFP polarization analyzers basis, which is spatially and periodically repeated all along the polarization state detector (PSD). In Fig. 1(a) we show the basic scheme that we consider in this paper, which is very similar to the device developed by Hsu *et al.* [10]. A pixelated retarder, the microretarder array (MRA), is stacked onto a polarizer overlaid onto the pixelated structure of the sensor camera. The pixels of the MRA coincide with the pixels of the sensor. We consider that the retardance is the same across the whole aperture and the alignment of the retarder neutral lines spatially vary —note that this system is equivalent to a polarimeter based on a rotating retarder [19] —, but without requiring mechanical movements. A

macropixel composed of four pixels in the MRA (i.e., the polarization analyzer basis) is necessary to obtain the Stokes vector of the fragment of light incident to the macropixel. Note that in DoFPs we sacrifice spatial bandwidth to obtain snapshot measurements. In fact, the spatial resolution of the polarimeter is limited by the 2×2 analyzer macropixel aperture. Each of the four elements in the macropixel is a different polarization analyzer so that only one measurement is produced on each pixel sensor. When considering the values of the other 3 neighboring pixels, then we obtain the full Stokes vector.
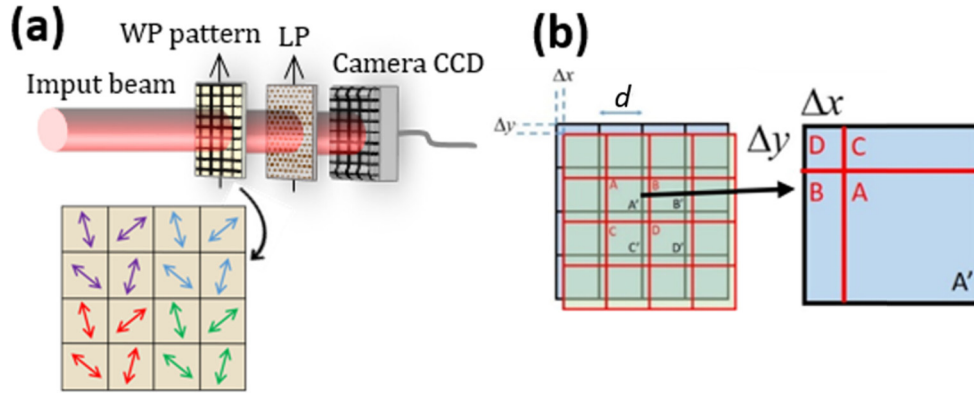

Fig. 1. (a) Scheme for a DoFP with the MRA. Black arrow shows a detail of four macropixels (labeled by four different colors); (b) Scheme of the misalignment between the pixelation of the microretarder (red) and the pixelation of the camera sensor (black).

Let us name $\vec{A}, \vec{B}, \vec{C}, \vec{D}$ the Stokes vectors associated with the pixel apertures of the MRA for the four analyzers composing the macropixel (red squares A, B, C, D in Fig. 1(b)). They are fully polarized states. In accordance with Fig. 1(b), let us consider some misalignment between the MRA pixels and the sensor pixels, across the horizontal Δx and the vertical Δy directions, and for a sensor pixel size d. Then the four pixel apertures of the MRA have a partial overlap along each of the camera sensor pixels. This defines a 2×2 macropixel structure which repeats across the sensor, which are the black squares A', B', C', D' in Fig. 1(b).

That is, the actual four Stokes analyzers of the analyzer basis can be written as a linear combination of the Stokes analyzers for a system without misalignments, resulting in the following four primed analyzers:

$$
\begin{aligned}
\vec{A}' &= p_1\vec{A} + p_2\vec{B} + p_3\vec{C} + p_4\vec{D} \\
\vec{B}' &= p_2\vec{A} + p_1\vec{B} + p_4\vec{C} + p_3\vec{D} \\
\vec{C}' &= p_3\vec{A} + p_4\vec{B} + p_1\vec{C} + p_2\vec{D} \\
\vec{D}' &= p_4\vec{A} + p_3\vec{B} + p_2\vec{C} + p_1\vec{D}
\end{aligned}
\tag{1}
$$

where the coefficients p_i express the spatial contribution of the each of the four detector states as follows,

$$
\begin{aligned}
p_1 &= (d - |\Delta x|)(d - |\Delta y|) \\
p_2 &= |\Delta x|(d - |\Delta y|) \\
p_3 &= (d - |\Delta x|)|\Delta y| \\
p_4 &= |\Delta x|\,|\Delta y|
\end{aligned}
\tag{2}
$$

We note that the degree of the spatial contribution expressed by the coefficients p_i does not depend on the sense of the misalignment: that is why we express the displacements Δx and Δy in absolute values. We consider maximum misalignments along X and Y of a 10% of the size of the pixel, which are reasonable tolerances when constructing the detection system onto the camera sensor.

The resultant intensity values on the sensor pixels are given by,

$$\vec{I} = W\vec{S} \tag{3}$$

where W is the measurement matrix whose rows are given by the four actual analyzers (i.e., $\vec{A}'$, $\vec{B}'$, $\vec{C}'$, $\vec{D}'$), $\vec{S}$ is the column vector for the incident polarization state under measurement, and the resultant intensity values are arranged as column vector $\vec{I}$. Thus, by taking into account relations in Eq. (1), we see how for values of Δx or/and Δy different than 0, matrix W in Eq. (3) will describe a polarimeter based on partial polarized analyzers.

In experimental implementations, the measurement matrix W is calibrated by applying a series of known incident polarization states. A 6 SOPs basis quite used for measurement matrix calibration is: $(1,1,0,0)^T$, $(1,-1,0,0)^T$, $(1,0,1,0)^T$, $(1,0,-1,0)^T$, $(1,0,0,1)^T$ and $(1,0,0,-1)^T$ [18,22], where T states for vector transpose. Once W matrix is calibrated, inversion of Eq. (3) then provides the incident SOP as a function of the intensities measured for the four analyzers,

$$\vec{S} = W^{-1}\vec{I} \tag{4}$$

Due to the matrix inversion conducted in Eq. (4), for an optimum performance of polarimeters, in terms of noise amplification, the polarization analyzers of the system must be selected to determine a measurement matrix W as far as possible of singular matrices. This can be done by choosing a polarization analyzer basis minimizing the condition number [18,19] of matrix W. For a 4×4 polarimetric matrix, the minimum value for the condition number is $CN_{min}=\sqrt{3} = 1.7321$ [9,18,19], ensuring an excellent performance of polarimeters. However, most of polarimeters proposed in literature present condition numbers within the range [1.73-4], so CNs smaller than 3 can be considered in general as acceptable values, and provide performances suitable for most polarimetric applications.

3.   Results and discussion

In this section, we provide different simulations to analyze the effect of the spatial misalignments discussed in Section 2 on the performance of DoFP polarimeters. The study is conducted both for the monochromatic (3.1) and polychromatic (3.2) cases. In addition, a robustness study to manufacturing errors is also given in Subsection 3.3.

3.1.   *Monochromatic DoFP polarimeter*

Let us proceed with the numerical simulations. First thing we need to do is to calculate the system parameters (values for the common retardance Γ and the orientations ϕ_A, ϕ_B, ϕ_C, ϕ_D of the four pixel apertures A, B, C, D in the MRA) that lead to an optimum performance of the polarimeter. We assume an ideal linear polarizer with infinite extinction ratio. We first consider monochromatic illumination. We run a non-linear iterative procedure where the figure of merit to minimize is the CN for the measurement matrix W. The first simulation is conducted when the detection system has no misalignments, and thus the CN_{min} must be achieved. Since there are local minima producing CN values higher than CN_{min}, we launch the minimization procedure with different starting values. We have verified that with less than ten tries we obtain such CN_{min}. This optimum CN is obtained by solution sets where the retardance is $\Gamma = 131.8°$ and the orientation of the fast axes of the microretarders with respect to the transmission axis of the linear polarizer are $\pm 15.1°$ and $\pm 51.7°$ in coincidence with the discussion by Sabatke et

al. [19]. In the following we have chosen the following solution set:$\Gamma = 131.8°$, $\phi_A = -51.7°$, $\phi_B = +51.7°$, $\phi_C = -15.1°$, $\phi_D = +15.1°$. This solution parameters is used to construct the corresponding fully polarized $\vec{A}$, $\vec{B}$, $\vec{C}$, and $\vec{D}$ Stokes analyzers that appear in Eq. (1), and lead to the optimal instrumental matrix W (in terms of noise amplification). Note that this polarization basis defines a regular tetrahedron if represented onto the Poincaré sphere, which corresponds to an optimum polarimeter based on a basis of four polarimetric analyzers [19,23].

Afterwards, by setting a displacement between the pixelation of the CCD sensor and that of the microretarder (i.e., for $\Delta x \neq 0$ and/or $\Delta y \neq 0$), Stokes analyzers $\vec{A}$, $\vec{B}$, $\vec{C}$, and $\vec{D}$ are modified to $\vec{A}'$, $\vec{B}'$, $\vec{C}'$, and $\vec{D}'$, according to Eqs. (1) and (4). This modification also transforms the corresponding instrumental matrix W, which now includes partial polarized Stokes analyzers. This leads to the simulated CN maps in Fig. 2 (monochromatic case). Figure 2(b) shows the degree of polarization (DoP) as a function of the misalignment along the X and the Y directions (for a maximum misalignment of 10%), averaged for the four polarization state detectors. As logical, for no misalignment the polarization analyzers are fully polarized and the averaged DoP is one (bottom-left corner). Conversely, the larger the misalignment, the smaller the DoP, with a minimum value of 0.75 (upper-right corner). In Fig. 2(d) we show the plot corresponding to the averaged DoP when there is only X-misalignment, Δx. We see that the values decrease to about 0.87.
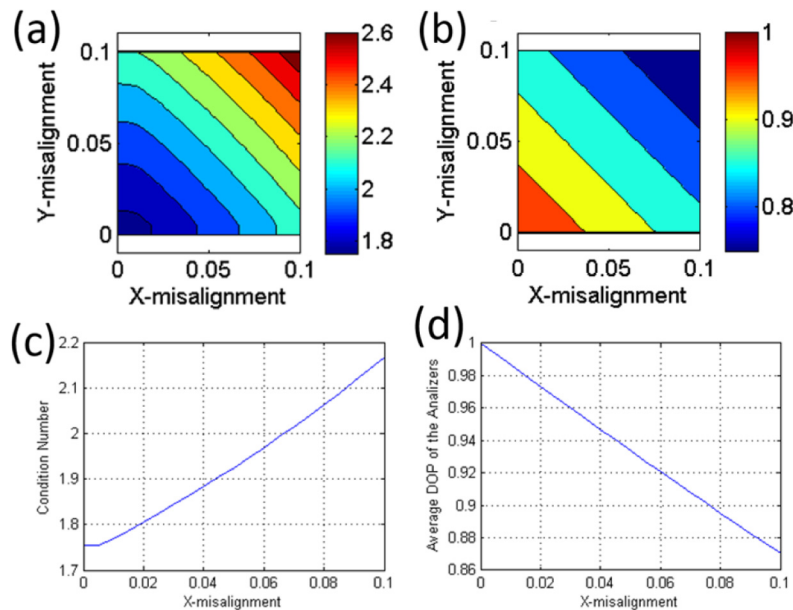

Fig. 2. (a) CN map obtained as a function of the X and Y misalignments; and (c) CN map for the particular case where $\Delta y = 0$. (b) Average DoP for the 4 analyzers as a function of the X and Y misalignments; and (d) Average DoP for the particular case where $\Delta y = 0$; Monochromatic case.

In Fig. 2(a) we show the CN of the W analyzers matrix as a function of the X and Y misalignments, where we see how the CN increases from the minimum possible value, 1.73 (bottom-left corner; when there is no misalignment), to a maximum value about 2.6 (upper-right corner), for the range considered of 10% of the size of the pixel. As stated before, CN values smaller than 3 are accurate enough for most applications, as the detection is still robust to noise amplification. In Fig. 2(c) we show the cut along the X-misalignment when $\Delta y = 0$ and we see that CN increases from 1.73 monotonically till about 2.2. Results in Fig. 2 show how misalignments

between MRA pixels and sensor pixels lead to DoFP polarimeters based on partially polarized analyzers (Figs. 2(b) and (d)). What is more, when these misalignments are smaller than 10%, the performance of the resulting polarimeters are still acceptable, in terms of error amplification (Figs. 2(a) and (c)).

Now we show the values for the equally weighted variance (EWV) [19] as a function of the X and Y misalignments. Together with CN, this figure of merit is commonly used to assess the noise amplification properties of polarimeters. In many instances it is more intuitive to interpret since it is directly related with a statistical concept. In Fig. 3(a) we show the EWV map of the *W* analyzers matrix as a function of the X and Y misalignments. We see an increase from 2.5 when there is no misalignment to a maximum of 4.4 (upper-right corner). Figure 3(b) shows the cut along the X-misalignment when $\Delta y = 0$, with a monotonous increase from 2.5 till about 3.3.
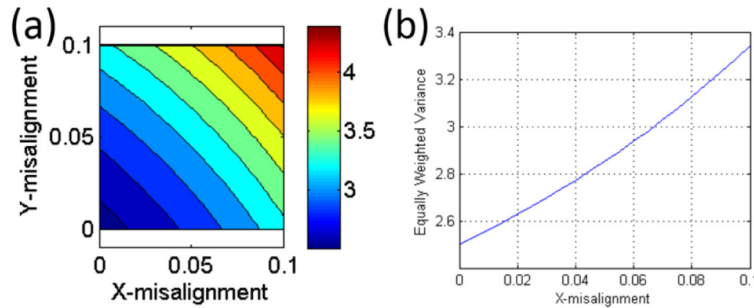

Fig. 3. (a) EWV as a function of the X and Y misalignments; and in (b) for $\Delta y = 0$. Monochromatic case.

3.2. *Polychormatic DoFP polarimeter*

In the literature, imaging polarimeters tend to be optimized for monochromatic illumination. However, there are many applications where it is interesting to obtain the polarimetric information for a series of illumination wavelengths, such as in [3,24]. Therefore, we also consider the case of polychromatic illumination, where various discrete wavelengths are applied sequentially. In particular, we consider wavelengths 625, 590, 530 and 470 nm, which sample the whole visible spectrum. In this case, our figure of merit is adapted to account for all the wavelengths tested. In particular, it is calculated as the condition number resultant from the addition of the CN given by each of the four wavelengths. We consider the following expression for the variation of the retardance as a function of the wavelength,

$$\Gamma(\lambda) = (2\pi/\lambda)\Delta n(\lambda)e \tag{5}$$

where *e* is the thickness of the MRA and Δn is the birefringence, which varies with the wavelength according to the dispersion function of the material composing the MRA.

For the purposes of this paper we approximate Δn as a constant, because variations of Δn as a function of the wavelength, in materials commonly used for composing MRAs, are usually small compared with the effect of the parameter λ in Γ. This does not reduce the generality of the conclusions obtained.

Since the retardance for the various wavelengths is fixed through Eq. (5), in the minimization procedure we have the same 5 degrees of freedom than in the monochromatic case. Once the retardance at one wavelength is obtained, the values at the other ones are simply scaled as,

$$\Gamma(\lambda_2) = (\lambda_1/\lambda_2)\Gamma(\lambda_1). \tag{6}$$

As in the monochromatic case, the minimization procedure needs to be launched from different starting values to avoid stagnation in a local minimum, moving away from the optimum CN

value. The optimum CN is produced by solution sets where the retardance at 625, 590, 530 and 470 nm is respectively 109.8°, 116.3°, 129.5° and 146.0°. In addition, the orientation of the fast axes of the microretarders with respect to the transmission axis of the linear polarizer are ±15.1° and ±51.5°. Note that the four above stated retardances obtained for the polychromatic case are different from the ideal value of 131.8° obtained in the monochromatic case (see section 3.1). In the same vein, the above shown orientations of the microretarders neutral lines, obtained for the polychromatic case, are slightly different from those that were obtained in the monochromatic case (i.e., ±15.1° and ±51.7°; see section 3.1). These optimized values differences between the monochromatic and polychromatic cases occur to compensate the polychromatic effect of illumination.

From the multiple solution sets, we show the results for $\phi_A = -15.1°$, $\phi_B = +51.5°$, $\phi_C = +15.1°$, $\phi_D = -51.5°$. In Fig. 4 we show the resultant polarization analyzer states on the Poincaré sphere. The four colors represent the four wavelengths considered. In each case, the corresponding tetrahedrons, whose vertices are defined by the 4 polarization analyzers, are also plotted. We note that as opposed to the monochromatic case discussed before, now these values do not represent the regular tetrahedron but a trade-off is found for the 4 wavelengths.
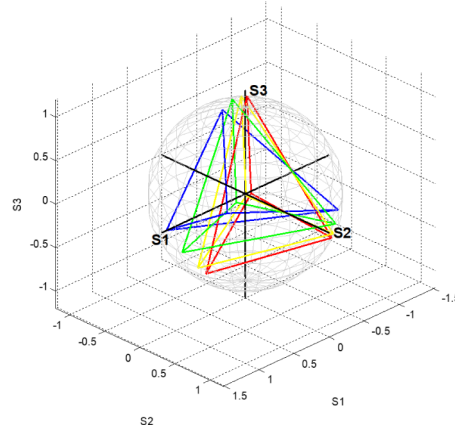

Fig. 4. Representation on the Poincaré sphere of the 4 optimal analyzers, where the 4 different colors indicates the 4 different wavelengths.

Now we show in Fig. 5(a)-(d) the contour plots for the DOP as a function of misalignment respectively for the wavelengths 625, 590, 530 and 470 nm. Within the 10% range of misalignment considered, the DOP values drop from 1 to about 0.75 in all the cases. When looked carefully, we see that contour maps for 625 nm (Fig. 5(a)) and 470 nm (Fig. 5(d)) are slightly asymmetrical with respect to X and Y misalignment. The retardance of the MRA at these wavelengths separates more from the ideal 131.8°, therefore the analyzer departure from the regular tetrahedron is responsible for this asymmetrical sensitivity to misalignment.

In Fig. 6(a)-(d) we show the CN as a function of misalignment and for the 4 wavelengths. The CN maps have a different shape and range of values for the 4 wavelengths. As numerical quantifiers of the polarimeter performance for those 4 wavelengths, we next provide, for each case, the values for two limit situations: (1) when there are no misalignments between the pixelation of the CCD sensor and that of the microretarder; and (2) for the maximum X-Y displacement. This data is given into parentheses, where the first number refers to the $\Delta x = \Delta y = 0$ situation and the second number to the $\Delta x = \Delta y = 0.1d$ situation. In particular, the CNs for these two limits cases are of (2.25; 2.87), (2.04; 2.65), (1.78; 2.62) and (2.32; 3.57), for the wavelengths 625, 590, 530 and 470 nm, respectively.
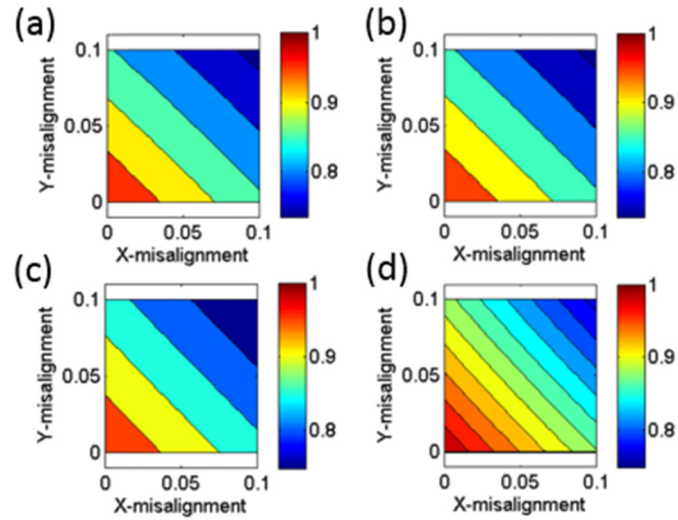
Fig. 5. Average DoP for the 4 analyzers as a function of the X and Y misalignment for: (a) 625, (b) 590, (c) 530 and (d) 470 nm.
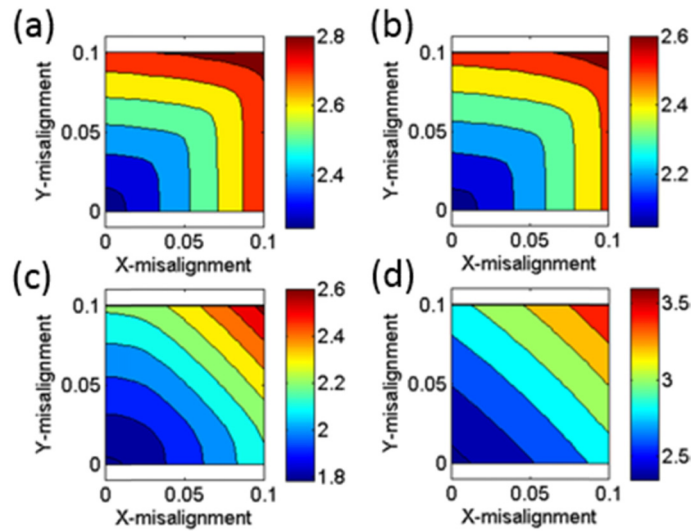

Fig. 6. CN for the 4 analyzers as a function of the X and Y misalignment for: (a) 625, (b) 590, (c) 530 and (d) 470 nm.

In case we want to obtain better results for the 470 nm, we simply have to increase the weight for this wavelength in the figure of merit for the minimization procedure. We checked this and obtained that this comes at the cost of increased CN values for 625 nm. As discussed with the DOP in Fig. 5, the CN maps shown in Fig. 6 lose in some cases the symmetry across the diagonal of the map, which means that it is not equal to have misalignment in X and Y. As in the monochromatic case, the partially polarized analyzers are very robust and within the 10% of misalignment the system produces a good imaging polarimeter.

Similarly, as in the previous figure for CN, now in Fig. 7(a)-(d) we show the EWV maps as a function of misalignment and for the 4 wavelengths. We see that the maps have a different range of values for the 4 wavelengths. We use the same quantifiers already defined in Fig. 6, so the EWV values we provide in parentheses correspond to the $\Delta x = \Delta y = 0$ situation (first number), and to the $\Delta x = \Delta y = 0.1d$ situation (second number). The EQW values for these two limiting cases are of (3.09; 5.16), (2.79; 4.71), (2.51; 4.39) and (2.83; 5.38), for the wavelengths 625, 590, 530 and 470 nm, respectively.
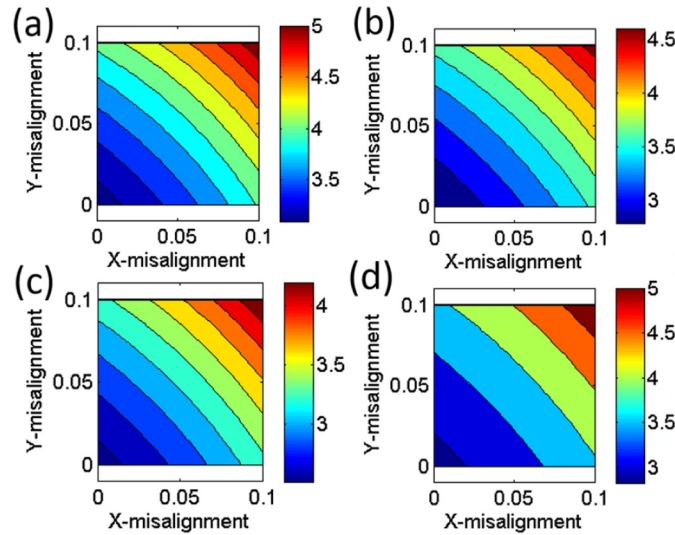

Fig. 7. EWV for the 4 analyzers as a function of the X and Y misalignment for: (a) 625, (b) 590, (c) 530 and (d) 470 nm.

We want to note that the analysis of DoFP polarimeters performance presented in this manuscript is limited to optimizing metrics that measure the noise amplification from intensity measures at the CCD camera to the final polarimetric measurements. However, MPAs were shown to be spatially-modulated channeled systems [20,25–27] and further analysis could be performed in a future based on Fourier-domain processing in order to study some considerations towards the effect of misalignment on the channeled nature of DoFP polarimeters.

3.3. Robustness to manufacturing errors

Now, we want to analyze robustness to manufacturing errors. Two main errors may be produced: deviations in the thickness of the MRA, where a $\pm 5\%$, i.e. about $\pm 5°$, is a reasonable tolerance, and deviations in the orientation of the neutral lines, where $\pm 1°$ is also a reasonable assumption. In the simulations we obtained that deviation in the retardance is more important than in the neutral lines. Let us show which are the best and worst values, i.e. the limiting cases, for the CN and the EWV within the range of 10% of misalignments along the X and the Y directions. In the case of positive deviations, +5% in the retardance and +1° in the neutral lines, then the best

(worst) CN values are 2.08 (2.70), 1.92 (2.55), 1.84 (2.85) and 2.85 (4.37) respectively for the wavelengths 625, 590, 530 and 470 nm. For the EWV the best (worst) values are 2.85 (4.80), 2.63 (4.49), 2.52 (4.52) and 3.40 (6.78) respectively for the wavelengths 625, 590, 530 and 470 nm.

In the case of negative deviations −5% in the retardance and −1° in the neutral lines, then the best (worst) CN values are 2.46 (3.10), 2.21 (2.83), 1.88 (2.54) and 1.99 (3.07) respectively for the wavelengths 625, 590, 530 and 470 nm. For the EWV the best (worst) values are 3.42 (5.67), 3.03 (5.06), 2.58 (4.44) and 2.58 (4.73) respectively for the wavelengths 625, 590, 530 and 470 nm. We see that in the case of positive deviations and negative deviations the most degraded wavelengths are respectively the 470 nm and the 625 nm, but still acceptable. Basically any combination of positive or negative deviations of the retardances produce CN and EWV values comprised within these two situations.

There are some other origins for overlap between the MRA and the sensor pixelation that we do not analyze in the paper but are worth mentioning: different size of the pixelation in both structures, and relative rotation between them. In these cases, the DOP would vary across the aperture of the MRA and CCD sensor and so would the CN and EWV do as well. In the present paper we have restricted our attention to the case of spatially invariant DOP, CN and EWV.

4. Conclusions

Under certain scenarios, usually related to experimental implementations, the actual polarimeters are based on partially polarized analyzers. This situation has been studied with a particular polarimeter case, the so-called division of focal plane (DoFP) polarimeters. These polarimeters are attracting high attention to polarimetric applications as they are snapshot polarimeters suitable to dynamic imaging.

In DoFP polarimeters, the partial depolarization is produced by misalignment between the pixelation of the CCD sensor and that of the microretarder (or the micropolarizer) array. We have provided a mathematical description showing the relation between spatial misalignments and the corresponding partial analyzers.

In addition, we studied the performance of DoFP polarimeters based on partial analyzers through a series of simulations. We showed how this system provides enough CN and EWV values to be considered for common polarimetric applications when misalignments between MRA and CCD sensor are restricted to values lower than 10%.

There are many applications where it is interesting to obtain the polarimetric information for a series of illumination wavelengths, and thus, the above-stated study was generalized to the polychromatic case. We showed the dependence of the resulting CN and EWV as a function of the wavelength, and how different performances are achieved by controlling the weight related to each wavelength considered. What is more, the performance of the resulting polarimeters is still acceptable under misalignments lower than 10%, for all the visible range.

Finally, to complete the error analysis, a discussion of the robustness to manufacturing errors achieved by polychromatic DoFP polarimeters is also provided.

References

1. M. Anastasiadou, A. De Martino, D. Clement, F. Liège, B. Laude-Boulesteix, N. Quang, J. Dreyfuss, B. Huynh, A. Nazac, L. Schwartz, and H. Cohen, "Polarimetric imaging for the diagnosis of cervical cancer," Phys. Status Solidi C **5**(5), 1423–1426 (2008).
2. K. M. Twietmeyer, R. A. Chipman, A. E. Elsner, Y. Zhao, and D. VanNasdale, "Mueller matrix retinal imager with optimized polarization conditions," Opt. Express **16**(26), 21339 (2008).

3. A. Van Eeckhout, A. Lizana, E. Garcia-Caurel, J.J. Gil, A. Sansa, C. Rodríguez, I. Estévez, E. González, J.C. Escalera, I. Moreno, and J Campos, "Polarimetric imaging of biological tissues based on the indices of polarimetric purity," J. Biophotonics **11**(4), e201700189 (2018).
4. L. J. November and L. M. Wilkins, "Liquid Crystal Polarimeter for solid state imaging of solar vector magnetic fields," in D. H. Goldstein and D. B. Chenault, eds. (International Society for Optics and Photonics, 1994), Vol. 2265, p. 210.
5. J. Hough, "Polarimetry: a powerful diagnostic tool in astronomy," Astron. Geophys. **47**(3), 3.31–3.35 (2006).
6. A. Márquez, I. Moreno, C. Iemmi, A. Lizana, J. Campos, and M. J. Yzuel, "Mueller-Stokes characterization and optimization of a liquid crystal on silicon display showing depolarization," Opt. Express **16**(3), 1669 (2008).
7. S. Firdous and M. Ikram, "Stokes Polarimetry for the Characterization of Bio-Materials using Liquid Crystal Variable Retarders," in Therapeutic Laser Applications and Laser-Tissue Interactions III (OSA, 2007), p. 6632_14.
8. E. Garcia-Caurel, R. Ossikovski, M. Foldyna, A. Pierangelo, B. Drévillon, and A. De Martino, "Advanced Mueller Ellipsometry Instrumentation and Data Analysis" in M. Losurdo and K. Hingerls, eds., (Springer-Verlag, 2013).
9. J. S. Tyo, D. L. Goldstein, D. B. Chenault, and J. A. Shaw, "Review of passive imaging polarimetry for remote sensing applications," Appl. Opt. **45**(22), 5453–5469 (2006).
10. W.-L. Hsu, G. Myhre, K. Balakrishnan, N. Brock, M. Ibn-Elhaj, and S. Pau, "Full-Stokes imaging polarimeter using an array of elliptical polarizer," Opt. Express **22**(3), 3063 (2014).
11. C. S. L. Chun, D. L. Fleming, and E. J. Torok, "Polarization-sensitive thermal imaging," Proc. SPIE **2234**, 275–286 (1994).
12. J. Guo and D. Brady, "Fabrication of thin-film micropolarizer arrays for visible imaging polarimetry," Appl. Opt. **39**(10), 1486 (2000).
13. V. Gruev, J. Van der Spiegel, and N. Engheta, "Dual-tier thin film polymer polarization imaging sensor," Opt. Express **18**(18), 19292 (2010).
14. H. Kikuta, H. Haccho, K. Iwata, T. Hamamoto, H. Toyota, and T. Yotsuya, "Real-time polarimeter with a form-birefringent micro retarder array," in K. Iwata, ed. (International Society for Optics and Photonics, 2001), Vol. 4416, p. 19.
15. X. Zhao, A. Bermak, F. Boussaid, and V. G. Chigrinov, "Liquid-crystal micropolarimeter array for full Stokes polarization imaging in visible spectrum," Opt. Express **18**(17), 17776 (2010).
16. G. Myhre, W.-L. Hsu, A. Peinado, C. LaCasse, N. Brock, R. A. Chipman, and S. Pau, "Liquid crystal polymer full-stokes division of focal plane polarimeter," Opt. Express **20**(25), 27393–27409 (2012).
17. N. Gu, B. Yao, L. Huang, and C. Rao, "Design and Analysis of a Novel Compact and Simultaneous Polarimeter for Complete Stokes Polarization Imaging with a Piece of Encoded Birefringent Crystal and a Micropolarizer Array," IEEE Photonics J. **10**(2), 1–12 (2018).
18. A. Peinado, A. Lizana, J. Vidal, C. Iemmi, and J. Campos, "Optimization and performance criteria of a Stokes polarimeter based on two variable retarders," Opt. Express **18**(10), 9815–9830 (2010).
19. D. S. Sabatke, M. R. Descour, E. L. Dereniak, W. C. Sweatt, S. A. Kemme, and G. S. Phipps, "Optimization of retardance for a complete Stokes polarimeter," Opt. Lett. **25**(11), 802 (2000).
20. A. S. Alenin, I. J. Vaughn, and J. S. Tyo, "Optimal bandwidth and systematic error of full-Stokes micropolarizer arrays," Appl. Opt. **57**(9), 2327 (2018).
21. F. Goudail and J. S. Tyo, "When is polarimetric imaging preferable to intensity imaging for target detection?" J. Opt. Soc. Am. A **28**(1), 46–53 (2011).
22. J. J. Gil and R. Ossikovski, "Polarized Light and the Mueller Matrix Approach," (CRC Press, 2016).
23. J. Scott Tyo, "Design of optimal polarimeters: maximization of signal-to-noise ratio and minimization of systematic error," Appl. Opt. **41**(4), 619–630 (2002).
24. M. Losurdo, M. Bergmair, G. Bruno, D. Cattelan, C. Cobet, A. de Martino, K. Fleischer, Z. Dohcevic-Mitrovic, N. Esser, M. Galliet, R. Gajic, D. Hemzal, K. Hingerl, J. Humlicek, R. Ossikovski, Z.V. Popovic, and O. Saxl, "Spectroscopic ellipsometry and polarimetry for materials and systems analysis at the nanometer scale: state-of-the-art, potential, and perspectives," J. Nanopart. Res. **11**(7), 1521–1554 (2009).
25. C. F. LaCasse, T. Ririe, R. A. Chipman, and J. S. Tyo, "Spatio-temporal modulated polarimetry," Proc. SPIE **8160**, 81600K (2011).
26. D. A. LeMaster and K. Hirakawa, "Improved microgrid arrangement for integrated imaging polarimeters," Opt. Lett. **39**(7), 1811–1814 (2014).
27. A. S. Alenin, I. J. Vaughn, and J. S. Tyo, "Optimal bandwidth micropolarizer arrays," Opt. Lett. **42**(3), 458–461 (2017).